Antiferromagnetic–paramagnetic insulating transition in Cr-doped V_2O_3 investigated by EXAFS analysis

C Meneghini[1,2]**, S Di Matteo**[3]**, C Monesi**[1]**, T Neisius**[4]**, L Paolasini**[5]**, S Mobilio**[1,2,6]**, C R Natoli**[6]**, P A Metcalf**[7] **and J M Honig**[7]

[1] Dipartimento di Fisica 'E Amaldi', Università di Roma TRE, via della Vasca Navale 84, I-00146 Roma, Italy
[2] TASC-CNR c/o OGG-GILDA ESRF, Polygone Scientifique Louis Néel, 6 rue Jules Horowitz, F-38000 Grenoble, France
[3] Equipe de Physique des Surfaces et Interfaces, Institut de Physique de Rennes UMR UR1-CNRS 6251, Université de Rennes 1, F-35042 Rennes Cedex, France
[4] Université Paul Cézanne, Faculté des Sciences et Techniques, 13397 Marseille, Cedex 20, France
[5] European Synchrotron Radiation Facility (ESRF), Polygone Scientifique Louis Néel, 6 rue Jules Horowitz, F-38000 Grenoble, France
[6] Laboratori Nazionali di Frascati INFN, via E Fermi 40, I-00044 Frascati, Roma, Italy
[7] Department of Chemistry, Purdue University, West Lafayette, IN 47907, USA

E-mail: meneghini@fis.uniroma3.it

Abstract
We have performed extended x-ray absorption fine-structure (EXAFS) spectroscopy on a 2.8% Cr-doped V_2O_3 sample, with the aim of studying its structural evolution in a wide temperature range across the paramagnetic–antiferromagnetic insulating phase transition at T_c. The data were registered with two different set-ups in fluorescence and transmission geometries, for polarized and unpolarized spectra, respectively. Our idea, based on previous experiments reported in the literature, is that extended structural modifications of the nominal trigonal symmetry are present in the paramagnetic insulating phase for several tens of degrees above T_c, involving further-nearest-neighbor vanadium ions. Our data confirm that the paramagnetic insulating phase is not structurally homogeneous in a temperature range of about 30 K around T_c, where local distortions of monoclinic symmetry involving further-nearest neighbors are present. Moreover, the analysis of the absorption profile at Cr K-edge suggests that Cr ions enter the lattice randomly. We finally analyze our findings in light of current theoretical models.

(Some figures in this article are in colour only in the electronic version)

1. Introduction

V_2O_3 has been the subject of considerable experimental and theoretical investigations for more than 40 years, in particular after its identification as the prototype of Mott–Hubbard systems [1]. Despite the quantity of experimental data available [2–10] and the amount of theoretical studies that followed [11–17], its structural, electronic and magnetic properties are still the subject of intense scientific debate [18, 19].

According to McWhan *et al* [2], the phase diagram of the stoichiometric compound is characterized by (i) a paramagnetic metallic (PM) phase at room temperature, with a corundum cell (rhombohedral system, $R\bar{3}m$), characterized by a threefold symmetry axis at vanadium sites, $\hat{C}_3$; (ii) a paramagnetic insulating phase (PI) at higher temperature (above $\simeq$500 K) and (iii) an antiferromagnetic insulating (AFI) phase at lower temperature (below $\simeq$160 K). Associated with the PM–AFI transition there is also a structural transition from rhombohedral to monoclinic symmetry ($I2/a$ group)

associated with a large (3.5%) volume expansion in the AFI phase that is responsible for the cracking of the single crystal when cooling it from the PM to the AFI phase. In [4], the existence of another, higher temperature metallic phase (PM′) was pointed out. The substitution of vanadium with chromium or aluminum forces the system into the PI phase even at room temperature. In the case of $(V_{1-x}Cr_x)_2O_3$, a value of $x \sim 0.02$ is sufficient to get a direct PI to AFI transition, without passing through the metallic phase [2]. In this case the PI–AFI transition temperature rises to $T_c \sim 180$ K and the transition itself is no longer disruptive.

As reviewed, for example, in [12], all transitions are often interpreted as due to the interplay between band formation and electron Coulomb correlation. We might safely say that the original idea of V_2O_3 as a Mott–Hubbard system [1], though modified after further experimental evidence already in 1973 [20], has survived in some cases up to the present [21]. The only fundamental modification of the original idea consisted in the introduction of the orbital degrees of freedom as basic ingredients to describe the phase diagram, (in 1978 by Castellani *et al* [11]). However, already in [11], the monoclinic distortion turned out to be fundamental for stabilization of the AFI phase, which showed that a purely electronic mechanism based on the Hubbard Hamiltonian was untenable and that lattice degrees of freedom played an important role. This idea has been revitalized theoretically in the last few years in revised forms [14, 15, 18], after the model of 1978 [11] needed to be corrected when two independent experimental studies showed that the average spin value on each vanadium ion is $S_V = 1$ [9, 10], contrary to the previously adopted value of $S_V = 1/2$ [11].

Notwithstanding the large harvest of experimental data and theoretical investigations about V_2O_3, we feel that several open points about its phase diagram are still present: those representing the main motivation for the present work are discussed in section 2. In section 3 we describe the experimental set-up for the two EXAFS (extended x-ray absorption fine-structure spectroscopy) data collections (both in fluorescence and in transmission geometry). Section 4 is dedicated to the data analysis: in order to keep full track of the adopted procedure to obtain our results, the latter is described in some detail, according to the guidelines of the XAS (x-ray absorption spectroscopy) Standards and Criteria Committee [22]. In section 5 we discuss our EXAFS results and compare their implications in light of previous experiments on the PI–AFI transition [23]. Section 6 is devoted to the analysis of the Cr K-edge absorption spectroscopy, in order to extract a possible model for the chromium distribution within the V_2O_3 lattice. Finally, in section 7 we discuss a possible interpretation of the present findings.

2. Motivation for the present work

In [24] a resonant x-ray scattering (RXS) experiment was performed at the V K-edge in a 2.8% Cr-doped V_2O_3 sample (the same crystal as in the present study). In particular, the temperature dependence of the $(00.3)_h$ resonant x-ray reflection ($(111)_t$ in trigonal settings) was analyzed in both the PI and AFI phase. As shown in [25] for the specific

case of V_2O_3, general symmetry arguments allow us to deduce a simple selection rule for RXS at the V K-edge for the $(111)_t$ trigonal reflection. In fact, insofar as the $\hat{C}_3$ axis is an exact symmetry at V sites, dipolar transitions are strictly forbidden and quadrupolar transitions are characterized by a threefold azimuthal modulation. Therefore the detection in [24] of a signal at dipolar energies (between 5470 and 5490 eV) above $T_c \simeq 180$ K is a clear indication that the threefold symmetry is lost as a point symmetry at V sites, even in the nominally corundum phase. In spite of these findings, an apparent contradiction seems to be present in the temperature range from 180 to ∼200 K: the measured threefold azimuthal scan at the energy of 3d states (around 5465 eV) seems to suggest that 3d states are still subject to a trigonal field without monoclinic distortion. This fact led us to suspect that there are two different length scales involved in the transition process: as dipolar 4p orbitals are more extended than quadrupolar 3d ones, there is a larger length scale where the $\hat{C}_3$ symmetry is lost even for $T \geqslant T_c$ and a local length scale where the $\hat{C}_3$-symmetry is still present down to T_c. We notice that the magnetic transition temperature $T_c \simeq 180$ K has been measured as the temperature at which AFM Bragg peaks appear.

Such considerations have driven our investigations towards the search for a quantitative deviation from the trigonal symmetry, even above T_c, possibly determined by further-nearest neighbors. We believe that, in order to explain the RXS experiment of [24], we are forced to consider the idea that locally (say, at the level of first-nearest neighbors) the point symmetry is C_3, but at the level of further-nearest neighbors such a symmetry is lost. It is important to notice, at this point, that both monoclinic and trigonal crystallographic cells of V_2O_3 are characterized by just one inequivalent site. Therefore it is not possible to have distortions of further-nearest neighbors without a correspondent distortion for nearest neighbors, unless we admit that in this temperature range atoms do not necessarily sit at the crystallographic sites. This implies that local structural modifications occur as 'atomic disorder' with short coherence length, in such a way that at a still larger length scale (hundreds of ångströms) the trigonal symmetry is restored. This would be in keeping with the coherence lengths measured in [24] by RXS.

We have therefore chosen EXAFS to investigate this matter: indeed, EXAFS technique is a unique tool to provide quantitative information on the atomic local structure around the absorber, which cannot be provided by RXS. Using a linearly polarized x-ray beam allows EXAFS to probe selectively structural features along specific directions in the sample. In this way we have been able to follow the structural changes across the PI–AFI transition along three independent crystallographic directions in the sample independently, i.e. along the corundum c_H axis and along two orthogonal directions in the hexagonal plane (see figure 1).

It is worthwhile at this stage to notice that two previous EXAFS measurements related to V_2O_3 have been reported in the literature. In [23] a polarized EXAFS study was performed on Al-doped V_2O_3 in both PI and AFI phases in order to analyze possible differences in their local structure. Even
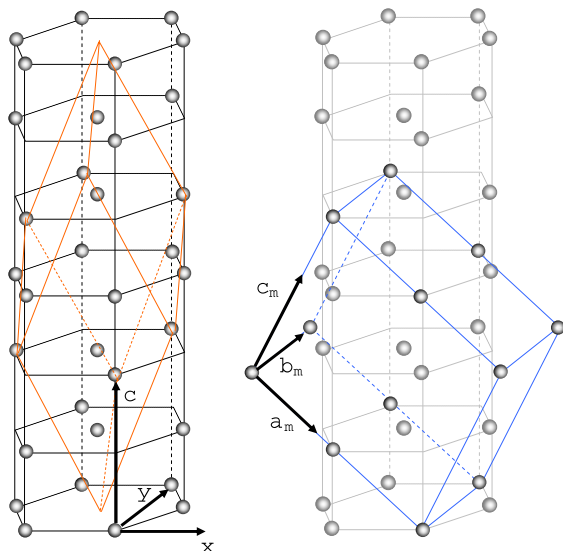
Figure 1. Schematic view of V_2O_3 structures: only V ions are shown for the sake of clarity. Left: the hexagonal cell with the trigonal (primitive) cell inside; right: relationship between corundum (room temperature PM phase) and monoclinic (low temperature AFI phase) unit cells. X-ray absorption measurements were performed aligning the x-ray beam polarization along the three orthogonal directions of the hexagonal lattice: the **c** axis and, perpendicular to it, the **x** and **y** (corresponding to the monoclinic b_m axis, see the text) directions highlighted on the left.

Figure 2. Schematic view of the experimental set-up. Data were collected with x-ray polarization (ϵ) in the hexagonal plane ($\epsilon \perp c_H$), i.e. along x and y (top) and parallel to the hexagonal C axis c_H (bottom). The fluorescence emission was collected using two photodiodes (P).

though the AFI and PI phases were reported, respectively, as monoclinic and trigonal by x-ray diffraction studies [7], in [23] no evident differences were found for the local structure in the two phases and both were fitted better by the monoclinic structure than by the trigonal one. Even though we basically agree with the analysis of [23], two key ingredients were still missing in their treatment for a full characterization of the PI phase, i.e. a full temperature dependence study of the signal, and a comparative study of the behavior of first-and further-nearest neighbors. In particular, since the measurements of [23] in the PI phase were collected at a temperature (180 K) only 15 K above the transition temperature of their Al-doped compound (whereas those of [7] were performed at room temperature), the authors may have missed the point, suggested by RXS from [24], that the paramagnetic insulating crystal structure changes with temperature even within the PI phase. Other EXAFS measurements have been reported in the literature for the stoichiometric compound [19]: we shall comment on them in section 7, when we compare their conclusions to ours in order to characterize the differences between PI and PM phases.

3. Experimental set-up

In our experiment a 2.8% chromium-doped V_2O_3 single-crystal (about $5 \times 5 \times 2$ mm^3) sample was used. It is the same sample already used for the experiments performed in [9, 24, 26, 27]. The material was grown in a skull melter under a controlled atmosphere and slowly cooled. The single crystals were then harvested and annealed. X-ray absorption spectra at V K-edge ($E_0 = 5465$ eV) were
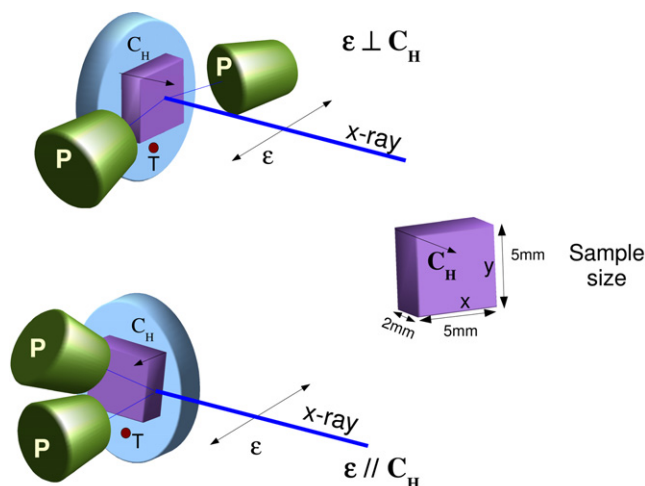
collected at the ID26 beamline of the European Synchrotron Radiation Facility (ESRF) in the fluorescence mode. The x-ray beam energies were selected using a double-crystal Si(220), fixed-exit monochromator, providing an energy resolution of $\sim$0.3 eV at the V K-edge. Energy scans were done in the so-called gap-scan mode, that is, tuning the maximum of the undulator emission to the actual monochromator rocking curve. Two mirrors provided an harmonic-free, small (diameter $\sim$300 μm), intense x-ray spot size on the sample, linearly polarized in the horizontal plane. The fluorescence intensity emitted from the sample was collected in the total-fluorescence mode by measuring the current from two photodiodes (figure 2), mounted parallel to the polarization of the incoming beam in order to minimize the elastic contribution to the spectrum and the self-absorption effect [28].

The 2.8% chromium-doped V_2O_3 single crystal was mounted in a closed-cycle He refrigerator for temperature scans between 100 K and room temperature. The sample temperature was continuously monitored using a K thermocouple mounted near to the sample ($\sim$5 mm). In order to exploit the directional sensitivity of polarized EXAFS, the absorption spectra were collected by correctly orienting the single crystal with respect to the linear polarization of the x-ray beam (figure 1).

Absorption spectra were collected in quick-EXAFS modes (20 s per scan) in the energy range 5300–6300 eV (about 4000 points per scan). The geometric set-up and the high energy resolution of the ID26 optic yielded very narrow Bragg peaks (few energy points) in the spectra. In order to remove them, for each temperature several (60–90) spectra were collected at different angles by rocking the sample ($\pm2°$) around the vertical axis. With this procedure Bragg peaks were shifted in energy along the spectra so that they could be easily singled out and removed. We could in this way register many scans, Bragg peak free, for each temperature point. The average of all the scans provided exceptional quality, low noise, XAS spectra suitable for accurate quantitative structural studies.
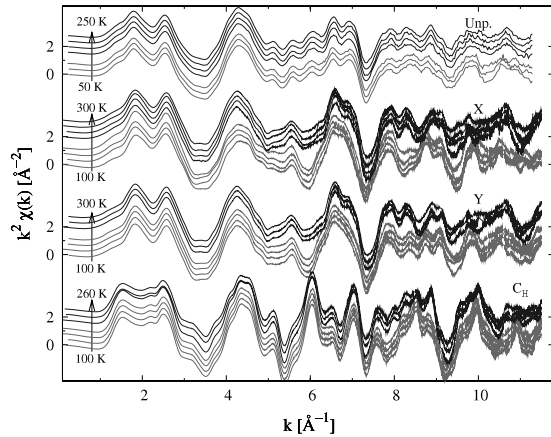
Figure 3. EXAFS data, k^2 weighted, as a function of temperature for unpolarized (Unp.) and polarized (X, Y and C) data. Data collected below the transition temperature ($T < T_c$) are shown in light gray, while in black are shown the EXAFS data collected above the transition temperature ($T > T_c$). The spectra are vertically shifted for the sake of clarity; an additional vertical shift is added to distinguish low temperature from high temperature spectra.

Temperature scans across the PI–AFI transition were collected with the x-ray linear polarization along the corundum c axis (C data in the following) and, in the hexagonal plane, along the monoclinic b_m axis (Y data) and orthogonal to it (X data). These two latter directions are shown in figure 1 as x and y, respectively. Note that we could definitively identify the single b_m axis out of the three possible twins as the direction in which we obtained the maximum in-plane linear dichroism (see [27] for further details).

As we are interested in the evolution of trigonal symmetry across the PI–AFI transition, we focused our investigation on the structure along the x and y directions. In particular, in order to accurately trace the structural changes across the PI–AFI transition, additional absorption spectra were acquired during sample cooling when the x-ray polarization was oriented along the **x** and **y** directions. The cooling speed of about 1 °C min^{-1} and the fast data collection (20 s) ensured good temperature stability during each scan. These data are taken by single scans for each temperature, which results in lower statistics.

The same data have already been used in [27] to prove the occurrence of structural dichroism in the XANES region. The reproducibility of the dichroic signal observed in the XANES region [27], as well in the extended region (raw EXAFS data in figure 3) ensures that all measurements were performed always in the same crystallographic domain.

The absorption spectra were calculated as $\mu(E) = I_f/I_o$, being the ratio between fluorescence intensity I_f and incident I_o. Self-absorption effects on $\mu(E)$ have been corrected using the program FLUO [29]. Note, however, that self-absorption only reduces the amplitude of EXAFS oscillations, leaving their phases unchanged. Therefore it mainly affects the coordination numbers and Debye–Waller factors but has no effect on interatomic distances. This is the reason why we will concentrate our discussion on interatomic distances, less affected by systematic errors.

We also collected further XAS data as a function of temperature (50–250 K) in the transmission mode on powder samples of the same composition at the BM29 beamline (ESRF). These data were collected on a sample prepared by grinding a small amount (∼10 mg) of one other 2.8% chromium-doped V_2O_3 single crystal. The powders were suspended in ethanol and homogeneously deposited on millipore membranes in order to obtain a homogeneous thin sample suitable for transmission experiments. Transmission geometry allows one to record EXAFS data of higher statistical quality (see figure 3), even though they are insensitive to polarization, due to the randomness of the grain orientation. These transmission data were used as a starting point in the EXAFS analysis in order to choose the main signals contributing to the vanadium absorption and to check the correctness of the self-absorption correction procedure.

4. Data analysis

Data analysis has been performed using the ESTRA and FITEXA programs [30]. Standard procedures were adopted for data normalization and extraction of the structural EXAFS signal: the pre-edge trend was simulated by a straight line and subtracted from the raw absorption spectra. The origin of the photoelectron energy scale (E_0) was chosen at the maximum of the first derivative of $\mu(E)$ and refined during the fitting (see below). The post-edge atomic absorption background (μ_0) was calculated by fitting a polynomial spline to the data in the k range 2–11.5 Å^{-1} (here $k = \hbar^{-1}\sqrt{2m(E - E_0)}$ is the photoelectron wavevector modulus with m: the electron mass and E_0 the V K-edge absorption edge energy). The k range is limited by the onset of the Cr K-edge ($E_{Cr} = 5989$ eV, i.e. $k \sim 11.8$ Å^{-1}). Note, however, that we were able to take advantage of the presence of the Cr K-edge, as described in section 6. The structural EXAFS signal was finally calculated as $\chi^{exp}(k) = (\mu(k) - \mu_0(k))/\mu_0(k)$.

The k^2 weighted EXAFS spectra, $k^2\chi(k)$, for unpolarized and polarized data are shown in figure 3. The moduli of Fourier transforms (FTs) of $k^2\chi(k)$ are shown in figure 4. The polarized spectra (figure 3) present larger structural features as compared with unpolarized data, which is also evident in the real space, as shown by the FTs (figure 4). The inspection of EXAFS spectra reveal that the X and Y data are often in antiphase with the C data (this is particularly clear in the regions around 6 Å^{-1} and around 9 Å^{-1}). The antiphase effect attenuates the structural features in the unpolarized spectra, weakening the next-neighbor peaks in the FTs.

Tuning the temperature across the PI–AFI transition the unpolarized and C data show weak effects both in k and in R space. In contrast, larger effects are visible on X and Y EXAFS spectra and their FTs: the latter directions have quite similar properties in the high temperature phase, as expected for the trigonal symmetry, but they are significantly different in the low temperature AFI phase (see, for example, the region around 8–9 Å^{-1} in figure 3), signaling the reduced symmetry of the monoclinic phase.

The major structural effects related to the PI–AFI transition are visible in the FTs of X and Y data, mainly,
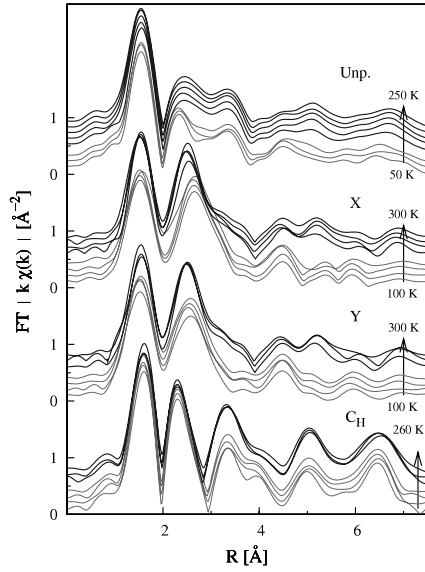
Figure 4. Moduli of Fourier transforms (FT) of k^2 weighted XAFS
data as a function of temperature for unpolarized (unp.) and
polarized (X, Y and C) experiments. Data collected below (above)
T_c are shown in gray (black) and vertically shifted for the sake of
clarity. The data are uncorrected for phase shift effect.

around 2.5 Å, and around 5 Å (a double-peak structure is
evident in the high temperature PI phase while a single peak
survives in the low temperature phase). In order to enhance our
sensitivity to the structural changes we decided to include in
the analysis the structural features up to about 6 Å. The effects
of transition are quite weak on the C_H data, confirming the
main structural effects related to the PI–AFI transition being in
the xy plane.

The data analysis was performed by fitting the k^2 weighted
EXAFS spectra directly in k space (i.e. without Fourier
filtering) including the main structural contributions (see
below) up to $R \sim 6$ Å. The theoretical EXAFS was modeled
with the standard formula [31, 32]

$$\chi^{\text{th}}(k) = S_0^2 \sum_i N_i \frac{A_i \sin(2kR_i + \phi_i)}{kR_i^2} \, e^{-2k^2/\sigma_i^2} \, e^{-2R_i/\lambda_i}$$

that is, a sum of contribution (shells) assuming a Gaussian
distribution of neighbors in each shell. The ith contribution is
characterized by three structural parameters: the coordination
number (or multiplicity number) N_i, the average coordination
distance (R_i) and the Debye–Waller factor σ_i^2 (being the
variance of the neighbor distribution). For unpolarized EXAFS
N_i represents the effective number of neighbors in the ith shell.
Dealing with polarized data an effective multiplicity number
N_i^* must be used instead, in order to take the directional
sensitivity of EXAFS into account: the contribution of the
jth neighbor in the shell must be weighted by the factor [33]
$3\cos^2\theta_j$, θ_j being the angle between the x-ray polarization
vector and the position vector $\vec{r}_j$ of the jth atom, with respect
to the absorber. In this way the closer the position vector
is to the polarization direction, the larger is its contribution
to the total EXAFS signal. No higher-order cumulants were

required for the data refinement[8]. Besides the structural
parameters, S_0^2 is a global factor taking into account many-
body losses that, after preliminary tests on unpolarized data,
we fixed at $S_0^2 = 0.85$. The $A_i(k)$ and $\phi_i(k)$ are, respectively,
the total amplitude and phase factor for the ith contribution
while $\lambda_i(k)$ is the energy-dependent photoelectron mean free
path. The photoelectron energy scale E_0 was initially refined
but we found it constant within 0.3 eV for all the spectra
(comparable with the energy resolution of the beamline optics),
so we kept it fixed in the definitive analysis. The $A_i(k)$,
$\phi_i(k)$ and $\lambda_i(k)$ were calculated by the FEFF8.2 [34] code,
using the complex Hedin–Lundqvist potentials in the muffin-
tin approximation. For theoretical amplitude and phase
calculations we used the monoclinic V_2O_3 structure as a
model of the low temperature phase and that of corundum
$(V_{0.972}Cr_{0.028})_2O_3$ for high temperature phase, both given
in [7]. Crystallographic structures were also used to group
neighbors in appropriate shells (figure 5) and to calculate the
(effective) multiplicity numbers (N_i^*) N_i that were kept fixed
in the fitting.

The EXAFS data were analyzed in the k range from 2.7 to
11.3 Å^{-1} according to the guidelines of the *XAS standards and
criteria committee* [22]. The fitting minimizes the k^n weighted
square residual function ($n = 2$ in our analysis):

$$\text{Res}^2_\chi = \frac{1}{N_p} \sum_j (k^n(\chi^{\text{th}}_j(k) - \chi^{\text{exp}}_j(k)))^2$$

where N_p is the number of experimental points. The fitting
quality was evaluated by the normalized residual function (the
so-called R factor [22]): $R^2 = N_p \text{Res}^2_\chi / W_o^2$ with: $W_o^2 = \sum_j (k^n \chi^{\text{exp}}_j(k))^2$. The R factor is in between 5 and 7% for
unpolarized data (measured in transmission) and fluorescence
data collected with higher statistics. It is around 10–15% in the
fast collected fluorescence scans (lower statistics).

The reduced χ_ν^2-like function:

$$\chi_\nu^2 = \frac{1}{N_p - N_{\text{par}}} \frac{\sum_j (k^n(\chi^{\text{th}}_j(k) - \chi^{\text{exp}}_j(k)))^2}{\sum_j k^{2n}\sigma_o^2}$$

was used to evaluate, through an F test, the statistical
significance of the considered contributions. σ_o^2 used to
evaluate the χ_ν^2 is the statistical variance of the experimental
data, which was evaluated by back Fourier filtering the high R
region ($R > 10$) of the experimental spectra, resulting in the
$1–7 \times 10^{-5}$ region.

An accurate analysis of the statistical errors was
performed using the MINUIT [35] capabilities, in order to
determine the confidence limits on the refined parameters and
the covariance matrix.

In the EXAFS data analysis the structural refinements
of next-neighbor shells is often a complex procedure which
necessarily involves several approximations. Indeed, many

---

[8] Concerning the use of cumulant expansion we highlight that it may help
in improving the data fitting, but it must be used with great care in order to
have physical significance. In particular the third-order cumulant is strongly
correlated (up to 80%) to the first one (being the interatomic distance R_j). We
checked that including the third-order cumulants in our analysis drastically
worsen the accuracy (error bar) on interatomic distances and gives poorly
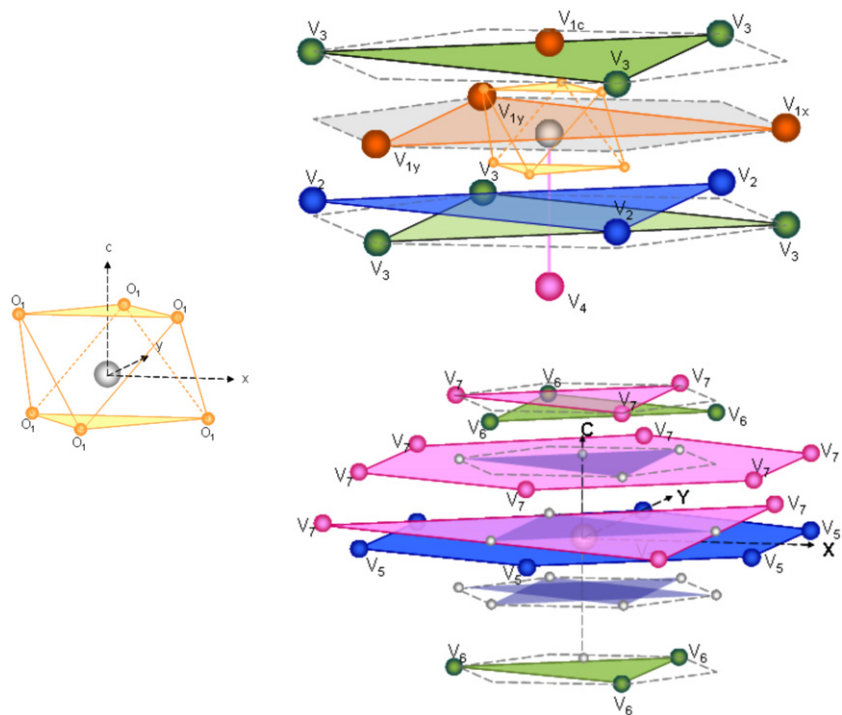reliable behavior.

Figure 5. Schematic view of neighbor shells used in the analysis of the data (grouped by color online). Upper: the V–O_1 nearest-neighbor shell, middle: the V_1 to V_4 neighbor shells, lower: the V_5 to V_7 shells. The planes of the hexagonal lattice are shown.
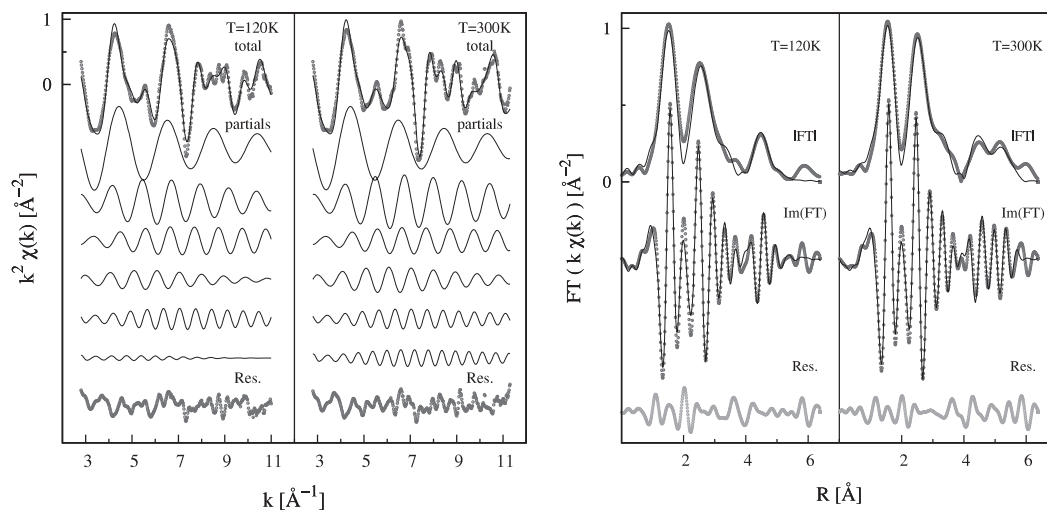

Figure 6. Example of V K-edge EXAFS data refinement at low (left panels) and high (right panels) temperatures (*Y* polarization): fitting of the whole EXAFS data (dots: experimental, line: theory), partial contributions and residuals (Res. = experimental theory) are shown (upper panels) shifted for clarity. The lower panels present the Fourier transforms of experimental (dots) and theoretical (line) k^2 weighted EXAFS spectra. Moduli, imaginary parts, and residuals are shifted for clarity.

contributions from single as well multiple scattering processes, may be negligibly weak due to interference from out-of-phase signals. This simplifies the analysis, allowing us to include a reduced subset of coordination shells that, however, must be selected with care. In this work the minimal set of contributions able to fit the data was determined after preliminary tests on unpolarized and polarized spectra far from T_c. The effective multiplicity numbers (N and N_j^*) were kept fixed to the values expected from the crystallographic structure, taking into account proper polarization corrections. The *F* test

was used in order to select the relevant contributions and to group together neighbor shells, i.e. a single shell was used (with cumulative coordination number and average distance) when the multi-shell model does not improve the fitting. The final signal subset used for the analysis is a result of an accurate trial-and-error procedure. Figure 6 schematizes the main coordination shells used in the analysis, the interatomic distances and the Debye–Waller factors are reported in figure 7. We used a structural model based on the monoclinic (trigonal) symmetry to fit the low (high) temperature data. In the
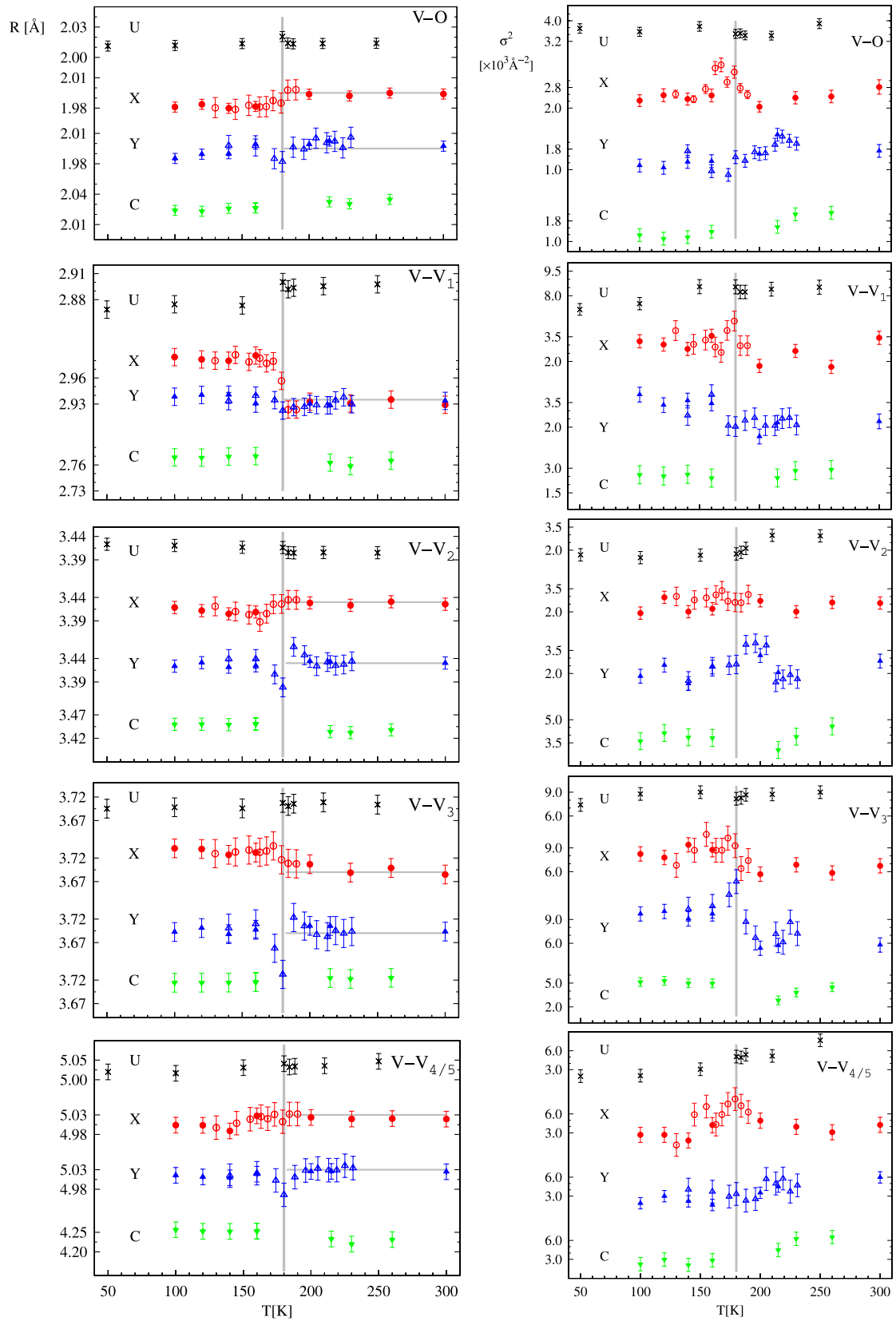
Figure 7. Coordination distances (left) and Debye–Waller factors (right) for the main contributions used in the V K-edge EXAFS data refinement are shown. The unpolarized U, (crosses: ×, black online), *X* (circles: ○, red online), *Y* (triangles: △, blue online) and *C* (triangles: ▽, green online) results for each shell are shown, shifted for clarity. For *X* and *Y* data filled (open) symbols represent the results of high (low) statistics spectra (see the text). The horizontal gray lines (left panels) represent the *X* and *Y* equal distances expected by assuming trigonal symmetry.

vicinity of the transition we checked which one (monoclinic or trigonal) was giving the best fit and we definitively found a better agreement of monoclinic (trigonal) below (above) the transition temperature T_c which, as stated above, we defined as the temperature at which the AFM Bragg peak appear. This definitively proves the sensitivity of our analysis in distinguishing the two structures. The effect of the phase transition on Debye–Waller factors is difficult to be interpreted: some of the σ_i^2 depict evident variations in the neighborhood of T_c while some others change weakly across the transition. Nevertheless it is evident that the changes in disorder also take place in a quite ample region around T_c, consistent with the hypothesis of a broad structural transition, at least from the local point of view. We also underline that in the refinement the correlations among Debye–Waller factors and the interatomic distances remain weak, less than 5–10 at.%, giving confidence on the obtained values.

A single shell is used to reproduce the V–O nearest-neighbor distribution, either for unpolarized and polarized spectra, even if the crystallographic structures provide different V–O_i bond lengths. In fact, the F tests demonstrate no statistical improvement if the V–O distribution was split. For unpolarized data the average R_{VO} observed are in good agreement with the crystallographic models. Dealing with polarized spectra, the oxygen ions will contribute differently to the total signal due to the different polarization factors and these factors change as a function of polarization direction. This is the reason why the measured R_{VO} along X and Y (C) are slightly shorter (longer) compared with the unpolarized case.

The next-neighbor EXAFS signals are dominated by V–V contributions, while we found negligible V–O and multiple scattering contributions (F tests). According to the crystallographic model of figure 5 the nearest V_o–V_1 shell is characterized by one V_1 ion (V_{1c}) along the hexagonal c axis at a shorter distance ($\sim$2.75 Å) and three V ions roughly within the hexagonal plane: one along the x direction (V_{1x}), and two (V_{1y}) at about $\pm120°$ from it. Fitting the unpolarized spectra we found that a single shell may be used to account for all four V_1 neighbors: using two shells, one for V_{1c} neighbor and one for the three V_{1xy} ions, does not improve the fitting (F test) but leads to unstable results. Concerning the polarized measurements the experimental geometry renders the C polarized data only sensitive to V_{1c}, the Y polarized data only sensitive to V_{1y} while both V_{1x} ($\sim$70%) and the two V_{1y} ($\sim$30%) contribute to the X polarized data.

Figure 5 schematizes the other V shells used in the analysis: V_2 (at $\sim$3.45 Å) and V_3 (at $\sim$3.7 Å) shells contribute to all the polarized signals (with different weights as a function of polarization). The V_4 ion (at $\sim$4.2 Å) is located along the hexagonal c_H axis, so it only contributes to the C polarized data; moreover, we found that it produces a negligible contribution to the unpolarized spectra. The V_5 ions (at $\sim$5 Å) are practically all located in the hexagonal plane; so the V_5 shell only contributes to the X and Y data. The V_6 ions (at $\sim$5.5 Å) contribute mainly to C polarized data, while V_7 ions (at $\sim$5.8 Å) contribute to all the polarized spectra with different weights (N_i^*). A maximum of seven contributions were used for each refinement and examples of EXAFS data fitting are shown in figure 6.

While refining the data the multiplicity numbers N_i^* were kept fixed at values calculated on the basis of monoclinic ($T < 180$ K) and trigonal ($T > 180$ K) structures. *A posteriori* we found that the relative behavior of interatomic distances is very weakly related to the trigonal or monoclinic model chosen to fix N_i^*: in fact, any differences in N_i^* are compensated for systematic changes of Debye–Waller factors. This is also the reason why we focused our discussion on the effect on interatomic distances and not on the model fitting. The interatomic distances and Debye–Waller factors were refined, resulting in a maximum of 15 free parameters in the refinements.

5. Results

Before discussing the structural results we feel it important to clarify again some points about the EXAFS data analysis. As stated above the analysis of EXAFS data, in particular when extended to the next-neighbor shells, necessarily requires approximations to reduce the number of free parameters in the fitting and their correlations. In this way it is possible to enhance the sensitivity of EXAFS to even very weak structural changes, by reducing the uncertainty on the refined parameters. The drawback of this approach is that the approximations made may reduce the absolute accuracy: for example, grouping several contributions in a single shell may induce systematic errors on the resulting average interatomic distances. Moving away from the absorber the approximations, which are mandatory for a reliable EXAFS data refinement (i.e. in our case neglecting multiple scattering terms and V–O contributions), become progressively more relevant. Therefore our quantitative analysis of the structural displacements might be affected by the neglected correlations. However, though each single atomic displacement should be taken with caution, their symmetry, on which our main result is based, is not under discussion: the x versus y symmetry breaking in the nominal corundum phase, mainly determined by further-nearest neighbors, is a robust feature of our analysis.

The interatomic distances for the first five coordination shells as a function of temperature and polarization are shown in figure 7: for unpolarized data the effects of the corundum to monoclinic transition are barely visible, especially for nearest neighbors. In contrast, more information can be deduced from polarized data, as detailed below.

The V_o–O_1 distances evolve weakly across the transition. The average V_o–O_1 distance along the C axis (close to 2.02 Å) is longer than along the x and y directions (both close to 1.99 Å). In the PI phase our results are in good agreement with those of the crystallographic structure [7]. In the AFI phase, however, there are some weak discrepancies, in particular for the V_o–O_1 distance measured with the Y polarization close to 2.00 Å, roughly unchanged across the PI–AFI transition. In contrast, the distance calculated on the basis of crystallographic data in the AFI phase leads to a value of 2.03 Å. This discrepancy may be due to Cr doping of our samples, while crystallographic data of the AFI phase refer to an undoped crystal.

The anisotropy at the transition for the V_o–V_1 structure is more marked, as deduced from the strong polarization dependence. First of all, the V_o–V_{1c} distance, around 2.76 Å, is largely temperature-independent, with room temperature and lower temperature values in agreement with those of [7]. Evidently, within the AFI phase, Cr doping has a lower influence on the V_o–V_{1c} distance than on V_o–O_1 distances. This aspect is important to frame our findings in a definite theoretical context, as detailed in section 7. The V_o–V_{1x} and V_o–V_{1y} distances are equal in the PI phase, as expected. The transition to the AFI phase elongates the V_o–V_{1x} bond, while the V_o–V_{1y} distance is practically unchanged (figure 7). Note that the Y data are determined by the V_o–V_{1y} distances alone: therefore the latter can be read directly from the plot. This is not the case for the V_o–V_{1x} elongation, as in the X data both V_o–V_{1x} (∼70%) and V_o–V_{1y} (∼30%) bonds are involved. Then the true V_o–V_{1x} elongation in the AFI phase is close to 2.99 Å.

All measured distances are, within several picometers, in agreement with those obtained by x-ray diffraction in [7]. Some slight differences could be attributed mainly to the Cr doping of our sample.

The constant value of V_o–V_{1y} and V_o–V_{1c} distances across the PI–AFI transition confirms [7] that the local modifications in the first vanadium shell consists of a tilting mode of the V_o–V_{1c} bonds, which rotate around the y axis (monoclinic b_m axis), moving towards the voids of the corundum structure and causing the elongation of V_o–V_{1x} bonds.

If we limit ourselves to room temperature and the lowest temperatures, then our EXAFS analysis is in general agreement with previous structural reports concerning the PI–AFI transition [7], and no further information is added. The relative changes at 100 and 300 K are rather limited for all V_o–V_2, V_o–V_3, V_o–V_4 and V_o–V_5 distances, especially along the c and y directions, whereas a relative change of the order of 1.2% is present for V_o–V_3 along the x direction: this latter corresponds to the tilting of the vertical axes in the lower and upper planes, which move in the same direction.

Definitely more interesting is, instead, the temperature dependence of the structural signal close to T_c, for which, to our knowledge, no data have been reported up to now in the literature for the Cr-doped samples. Our main interest, as explained in section 2, concerns further-nearest neighbors: it is indeed evident from figure 7 that structural rearrangements (of amplitude ∼2%) occur for third, fourth and fifth neighbors (V_o–V_2, V_o–V_3 and V_o–V_5) about the transition in a range of more than 20 K both above and below T_c (the nominal T_c of the sample from magnetic diffraction data is 180 K). Below T_c, these structural rearrangements become stable close to the nominal transition temperature of the stoichiometric compound (T_{cs} ∼ 150 K), whereas in the high temperature region they are non-negligible up to slightly above 200 K. These findings are a signature of the role of monoclinic correlations even above T_c, as the symmetry associated with the distortion of V_2, V_3 and V_5 ions evidently breaks the trigonal symmetry showing a definitely different behavior along the X and Y directions. This is particularly evident in the V_2–V_5 neighbors.

Following the discussion about the sensitivity and accuracy of EXAFS data analysis at the beginning of this section, we consider such displacements as an indication of the breaking of trigonal symmetry at the level of the further-nearest neighbors. Moreover, as such displacements correspond to the natural onset of the unique monoclinic axis below T_c (b_m, along the y direction), we can affirm that the system has already determined its monoclinic unique axis (out of three) at least 20 K above the magnetic (and transport) transition temperature. This choice is not determined by the vertical axis tilting, as the V_0–V_1 bond along the x direction is unchanged, but by the further-nearest-neighbor rearrangements.

6. Cr K-edge

The possibility of two distinct, spatially isolated phases has driven us to investigate the effects of Cr ions on the local symmetry, through an analysis of the Cr K-edge XANES (x-ray absorption near-edge structure) profile, with the idea in mind that Cr ions might form impurity centers that determine the inhomogeneity at low T. It is interesting to note in this respect that, in spite of the huge literature on V_2O_3, very little is known about the role of chromium in the lattice. For example, though it appears reasonable to assume (as always in the literature) that Cr ions enter the lattice substitutionally, as it is in the case of Fe^{3+} ions where such an analysis is made possible by Mössbauer spectroscopy [36], to our knowledge no such experimental proof exists in the literature for chromium. Another important missing piece of information involves the analysis of the Cr-ion distribution (random or correlated clusters), which can affect the electron energy distribution. Indeed, the interesting theoretical analysis to investigate the influence of Cr doping on the electronic density of states through the coherent potential approximation [18] is based on the hypothesis that Cr^{3+} ions are randomly distributed in the crystal. Actually, at the beginning of the 1970s, several papers [20, 36, 37] were investigating the role of impurities in the phase diagram of V_2O_3. In particular Brinkman and Rice [37] performed a theoretical analysis with a Gutzwiller-type approach to calculate the residual resistivity in Cr-doped samples: they found that it should have been bounded, yet this upper bound was violated in Cr-doped samples (see figure 12 of [20]). In practice, all that work could not really resolve this problem and it was customary to get rid of it qualitatively by stating that the role of chromium is to increase the average cation–cation distance ($\Delta V \simeq 0.39$ cm^3 mol^{-1}) [11], which leads to a mechanism for the metal–insulator transition traditionally described by Mott [38]. However, the mechanism behind the localization of the two 3d electrons of V^{3+} ion in the PI phase is probably more determined by the relative position of electronic levels of the V^{3+} ions and Cr^{3+} ions. In fact, each Cr^{3+} ion carries three 3d electrons occupying the t_{2g} subband, coupled to produce a spin 3/2, according to the intra-atomic Hund's rule. To put another electron on a site occupied by a Cr ion would require a much higher energy, given the large value of the Hund's coupling constant presently accepted [13], $J \simeq 1$ eV[9]. For this reason, a Cr-occupied site has to be

---

[9] An exhaustive analysis of the possible values of Hund's coupling constant can be found in section IV of the first of [15].
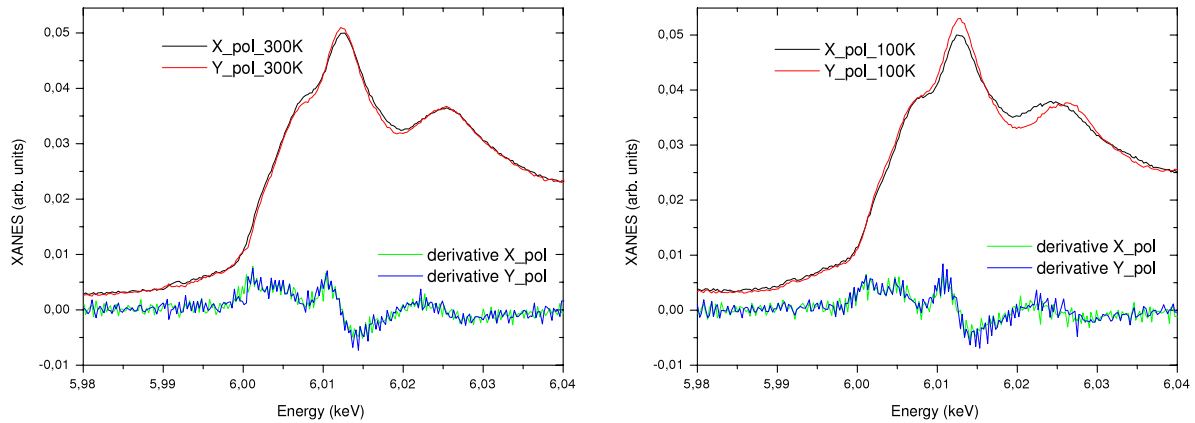
Figure 8. Cr K-edge XANES at 300 K at 100 K. For each temperature, we show *X* and *Y* polarization measurements and their derivatives, to highlight the absence of a pre-peak around 5.99 keV.

counted as a site onto which the V 3d electrons cannot jump, due to the presence of an effective repulsive potential barrier. Hence, increasing the Cr percentage leads to an effective reduction of conductivity. If this were the case, we would be confronted with a percolation problem (not a Mott–Hubbard one!) and, in this respect, it would be interesting to know not only whether Cr^{3+} ions enter the lattice substitutionally (which appears plausible and is implicit in the previous argument), but also whether they are distributed randomly in the crystal or whether a kind of local correlation sets in. In this case there is a strong probability that a Cr^{3+} ion has another Cr^{3+} ion as first- or second-nearest neighbor. This would lead to the formation of clusters locally rich in chromium, which could represent a realization of the 'nucleation of locally insulating clusters leading to exceptionally large scattering centers' suggested in note 14 of [37] to explain the residual resistivity of Cr-doped samples, which had been left unexplained within a Gutzwiller-type electron-correlated approach [37].

In order to settle this problem, we performed near-edge absorption measurements at the Cr K-edge, after proper subtraction of the EXAFS signal of the V K-edge. Our idea is that quantitative indications of Cr positions can be extracted from the Cr K-edge XANES signal. This concept was supported by a series of previous numerical calculations performed with the FDMNES program in the multiple scattering mode. A detailed explanation of the FDMNES program can be found in [39]: a specific application of FDMNES to the case of V_2O_3 is described in detail in [40]. We considered several V_2O_3 Cr-doped clusters characterized by the presence of one or more Cr^{3+} ions in different lattice positions. Such spectra showed obvious differences at their pre-edges. We considered V_2O_3 clusters of 135 atoms (cluster radius 6.9 Å) in the following configurations:

  (a) one Cr atom per unit cell (the absorbing atom, at the V_0 site);
  (b) two Cr atoms per unit cell: in this case the calculations differ according to the position of the second Cr atom that replaces a vanadium atom at each inequivalent site;
  (c) non-substitutional Cr atoms, placed 'elsewhere' (other than at vanadium lattice sites) in the corundum cell.
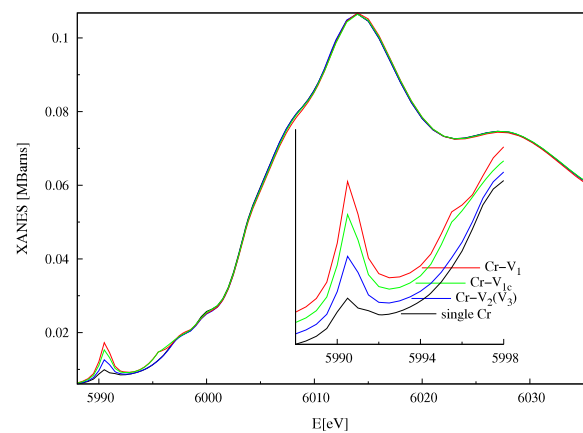

Figure 9. Theoretical calculation of the Cr K-edge XANES (see the text). The inset highlights the effect of different Cr configurations in the pre-edge region.

We analyzed several spectra of this latter configuration and found them profoundly different from the experimental ones, shown in figure 8, for the presence of some extra 'bumps' in the region between the pre-edge and the edge regions, thereby excluding this case. In contrast, the two calculations of cases (a) and (b), shown in figure 9, compare rather well with the experiment. The two cases (a) and (b) represent, respectively, the random configuration of Cr^{3+} ions in the lattice (with 2.8% Cr doping there is, on average, about one atom in a monoclinic cell) and a Cr-correlated cluster, simulating the higher probability of Cr^{3+} ions staying closer together. The good qualitative agreement of cases (a) and (b) with the experimental spectra, compared with the very bad agreement of (c), simply allows us to conclude that Cr^{3+} ions enter the lattice substitutionally.

We may then turn to the main difference between cases (a) and (b), in the pre-edge region: if we consider just one Cr atom per unit cell, then only a very low feature should be present at about 10 eV below the main edge, whereas if we add a second Cr atom in the cell, by increasing the local density of Cr atoms, a very sharp peak should appear around 5.99 keV, probably due to the increased inversion symmetry breaking

around the Cr site. We can compare this behavior with the experimental spectra, which show no pre-peak features (as evidenced by their first derivative) and therefore conclude that this is the signature of a random configuration of Cr^{3+} ions in the lattice. A quantitative analysis of the pre-peak would not be conclusive, because of the uncertainty arising from the V K-edge EXAFS subtraction, which, while leaving us qualitatively confident about the absence of general Cr–Cr correlation clusters, does not allow us to estimate a precise upper bound for it.

7. Discussion and conclusions

The main results of our work are:

(a) There are structural distortions in cooling from the PI to the AFI phase which break the trigonal symmetry at least 20 K above T_c: the PI phase, therefore, is not trigonal over the whole temperature range.

(b) The atoms associated with these distortions are not the first neighbors which do not move appreciably down to the transition temperature, but further-nearest neighbors: they act locally as an effective monoclinic field and, when they reach a critical value they drive the magnetic phase transition at T_c. The fact that further-nearest neighbors move, whereas first-nearest neighbors do not, implies that some structural disorder is present in this temperature range and vanadium ions do not necessarily all sit at crystallographic positions.

(c) Cr impurities enter the lattice substitutionally and in random configurations: this excludes the possibility of formation of large insulating clusters related to Cr doping [37] and supports theoretical approaches like the CPA [18].

Findings (a) and (b) are in agreement with the qualitative RXS observations of [24]: in that paper a different full width at half-maximum (FWHM) was measured at $T \simeq 183$ K for two peaks of the same family (e.g. $(111)_t$ and $(333)_t$). For an ideal lattice the two peaks should obviously have been equal; however, for a non-ideal lattice, the reflection with the larger exchange vector $\vec{Q}$, $(333)_t$, is more sensitive to longer-range distortions. Therefore, its larger FWHM is coherent with our interpretation.

Moreover, our results can be combined with those of [19] on the stoichiometric compound to single out general characteristics of the paramagnetic-to-antiferromagnetic transitions (from both PM and PI phases): these two transitions appear when the vertical molecule is both tilted and elongated ($d \simeq 2.75$ Å). The analysis of [19] did not extend to further-nearest neighbors: however, it clearly showed structural in-plane transformations that led to the magnetic and transport transition only at the temperature where the vertical molecule reached the elongated, tilted position, and not at the higher temperature where the molecule reached its maximum tilting angle but was not elongated yet. In our Cr-doped sample, *mutatis mutandis* (the vertical molecule is already elongated around $d \simeq 2.75$ Å, even in the high temperature phase), the phase transition corresponds to the temperature at which the vertical molecule goes

into its tilted, elongated configuration, whereas some 'precursor' phenomena to be identified below appear even above T_c.

A possible realization of the transition mechanism is indicated by A. Tanaka in [16] and based on the 'vertical' molecule V_0–V_{1c}. Such a model allows us to explain the phase diagram of the system in terms of the different hybridization of two molecular electronic states that are very close in energy, and identified by the different e_g^π:a_{1g} ratios. In this theoretical framework it is the length of the V_o–V_{1c} bond that controls the metallic or insulating character of the system: such a length is a binary variable that changes abruptly between two potential minima at about 2.75 Å for the insulating phase and about 2.70 Å for the metallic phase. The shorter bond length of the vertical molecule corresponds, as experimentally found, to the higher value of the a_{1g} percentage in the wavefunction ($\sim$25%). Such states are correctly characterized by a total spin $S = 1$ per V atom and an orbital angular momentum $L = -0.5$ μ_B, as experimentally found in [9]. Moreover, the introduction of a molecular spin, i.e. a spin state whose wavefunction extends over the whole molecule, can explain the absence of a spin component out of the glide plane on the basis of symmetry considerations [41], and the change in the orbital occupancy in the molecular wavefunction allows one to explain even the linear dichroism experiment of [10] (see figure 15 of [16]). The PI/AFI transition is described in such a model as an order-to-disorder transition, where each molecule can fluctuate in the high temperature phase between three positions that correspond to the three *a priori* equivalent monoclinic distortions of the molecule. On average, such fluctuations restore the trigonal symmetry that is indeed observed in the PI phase, because the three positions of the V_0 ion in the V_1 plane, at the vertex of an equilateral triangle, have an average distance that is equal to the exact (unmoved) trigonal position. We would like to stress that, if the vertical molecules flip randomly among these three positions, the average distance of V_0 to any other ion would correspond to the undistorted distance. Moreover, a situation where nearest-neighbor distances do not change and further-nearest-neighbor distances do change, as shown in our data, necessarily implies that we are dealing with dynamical variables and what we are sensitive to is some averaged position. In fact, V ions occupy a single nonequivalent Wyckoff site and there is no space for other solutions. This seems to point towards a pair correlation of molecules that break the trigonal symmetry, but more specific calculations should be developed before a firm statement in this direction is made.

For completeness, we should say that, focusing on photoemission experiments, V_2O_3 is often theoretically described by dynamical mean-field theory (DMFT) [42, 43], which can provide an alternative realization of the transition, not based on the vertical molecule. There is no overwhelming evidence favoring either of the interpretations: however, the experimental evidence presented in this work is naturally explained in the framework of Tanaka's model, which partly foresaw such behavior. Moreover, we are not aware of DMFT calculations that predict a non-negligible angular orbital moment, as experimentally found [9], and as easily described in the context of the vertical molecule. Probably

the realization of cluster calculations within DMFT, in order to handle correctly the dynamical and non-local correlations implicit in the molecular wavefunction, would be necessary for a proper interpretation of the V_2O_3 phase diagram. This will be extremely important if the tight-binding hopping parameters from the downfolding procedure of [44] turn out to be correct, as they drastically reduce the binding energy of the vertical molecule, thus implying its possible breakdown in the crystal ground state. If this is not the case, the molecular state will play an important role in the description of V_2O_3 phase diagram, given its strength even in the crystal lattice, as shown in [15].

Acknowledgment

References

[1] McWhan D B, Rice T M and Remeika J P 1969 *Phys. Rev. Lett.* **23** 1384
[2] McWhan D B and Remeika J P 1970 *Phys. Rev.* B **2** 3734
[3] McWhan D B, Remeika J P, Bader S D, Triplett B B and Philips N E 1973 *Phys. Rev.* B **7** 3079
[4] Kuwamoto H, Honig J M and Appel J 1980 *Phys. Rev.* B **22** 2626 and references therein
[5] Rosenbaum T F, Husmann A, Carter S A and Honig J M 1998 *Phys. Rev.* B **57** R13997
[6] Bao W, Broholm C, Aeppli G, Carter S A, Dai P, Rosenbaum T F, Honig J M, Metcalf P and Trevino S F 1998 *Phys. Rev.* B **58** 12727
[7] Dernier P D and Marezio M 1970 *Phys. Rev.* **2** 3771
[8] Moon R B 1970 *Phys. Rev. Lett.* **25** 527
[9] Paolasini L, Vettier C, de Bergevin F, Yakhou F, Mannix D, Stunault A, Neubeck W, Altarelli M, Fabrizio M, Metcalf P A and Honig J M 1999 *Phys. Rev. Lett.* **82** 4719
[10] Park J-H, Tjeng L H, Tanaka A, Allen J W, Chen C T, Metcalf P, Honig J M, de Groot F M F and Sawatzky G A 2000 *Phys. Rev.* B **61** 11506
[11] Castellani C, Natoli C R and Ranninger J 1978 *Phys. Rev.* B **18** 4945
    Castellani C, Natoli C R and Ranninger J 1978 *Phys. Rev.* B **18** 4967
    Castellani C, Natoli C R and Ranninger J 1978 *Phys. Rev.* B **18** 5001
[12] Spałek J 1990 *J. Solid State Chem.* **88** 70
[13] Ezhov S Y, Anisimov V I, Khomskii D I and Sawatzky G A 1999 *Phys. Rev. Lett.* **83** 4136
[14] Mila F, Shiina R, Zhang F-C, Joshi A, Ma M, Anisimov V and Rice T M 2000 *Phys. Rev. Lett.* **85** 1714
    Shiina R, Mila F, Zhang F-C and Rice T M 2001 *Phys. Rev.* B **63** 144422
[15] Di Matteo S, Perkins N B and Natoli C R 2002 *Phys. Rev.* B **65** 054413
[16] Tanaka A 2002 *J. Phys. Soc. Japan* **71** 1091
[17] Elfimov I S, Saha-Dasgupta T and Korotin M A 2003 *Phys. Rev.* B **68** 113105
[18] Laad M S, Craco L and Müller-Hartmann E 2006 *Phys. Rev.* B **73** 045109
[19] Pfalzer P, Obermeier G, Klemm M, Horn S and den Boer M L 2006 *Phys. Rev.* B **73** 144106
[20] McWhan D B, Menth A, Remeika J P, Brinkman W F and Rice T M 1973 *Phys. Rev.* B **7** 1920
[21] Allen J W 2005 *J. Phys. Soc. Japan* **74** 34
[22] *Error Reporting Recommendations: A Report of the Standards and Criteria Committee* 2002 http://ixs.csrri.iit.edu
[23] Pfalzer P, Will J, Nateprov A Jr, Klemm M, Eyert V, Horn S, Frenkel A I, Calvin S and den Boer M L 2002 *Phys. Rev.* B **66** 085119
[24] Bombardi A, de Bergevin F, Di Matteo S, Paolasini L, Metcalf P A and Honig J M 2004 *Physica* B **345** 40
[25] Di Matteo S, Joly Y, Bombardi A, Paolasini L, de Bergevin F and Natoli C R 2003 *Phys. Rev. Lett.* **91** 257402
[26] Paolasini L, Di Matteo S, Vettier C, de Bergevin F, Sollier A, Neubeck W, Yakhou F, Metcalf P A and Honig J M 2001 *J. Electron Spectrosc. Relat. Phenom.* **120** 1
[27] Meneghini C, Di Matteo S, Monesi C, Neisius T, Paolasini L, Mobilio S, Natoli C R, Metcalf P A and Honig J M 2005 *Phys. Rev.* B **72** 33111
[28] Booth C H and Bridges F 2005 *Phys. Scr.* T **115** 202
[29] Haskel D 1999 FLUO is available at http://depts.washington.edu/uwxafs/Tools/Tools.html
[30] Meneghini C, Bardelli F and Mobilio S ESTRA and FITEXA programs are available at http://webusers.fis.uniroma3.it/~meneghini/software.html
[31] Lee P A, Citrin P H, Eisenberger P and Kincaid B 1981 *Rev. Mod. Phys.* **53** 769
[32] Rehr J J and Albers R C 2000 *Rev. Mod. Phys.* **72** 621
[33] Koningsberger D C and Prins R 1988 *X-Ray Absorption* (*Chemical Analysis Series* vol 92) (New York: Wiley)
[34] Ankudinov A L, Ravel B, Rehr J J and Conradson S D 1998 *Phys. Rev.* B **58** 7565
[35] James F 1994 CERN 506 *Program Library*
[36] Wertheim G K, Remeika J P, Guggenheim H G and Buchaman D N E 1970 *Phys. Rev. Lett.* **25** 94
[37] Brinkman W F and Rice T M 1972 *Phys. Rev.* B **5** 4350
[38] Mott N F 1990 *Metal–Insulator Transition* (London: Taylor and Francis)
[39] Joly Y 2001 *Phys. Rev.* B **63** 125120
[40] Joly Y, Di Matteo S and Natoli C R 2004 *Phys. Rev.* B **69** 224401
[41] Di Matteo S 2005 *Phys. Scr.* **71** CC1-6
[42] Keller G, Held K, Eyert V, Vollhardt D and Anisimov V I 2004 *Phys. Rev.* B **70** 205116
[43] Poterayev A I, Tomczak J M, Biermenn S, Georges A, Lichtenstein A I, Rubtsov A N, Saha-Dasgupta T and Andersen O K 2007 *Phys. Rev.* B **76** 085127
[44] Saha-Dasgupta T, Nuss J, Andersen O K, Lichtenstein A I, Poterayev A I and Georges A, unpublished